


RESEARCH ARTICLE OPEN ACCESS

Porous Bi₂S₃ Bulk With Excellent Thermoelectric Performance by Solid States Replacement and Low Melting-Point Metal Volatilization

 Zi-Yuan Wang^{1,2} | Jun Guo¹ | Yi-Xin Zhang¹ | Hao Liang¹ | Xing Yang¹ | Rafal E. Dunin-Borkowski³ | Fengshan Zheng⁴ | Lei Jin³  | Jing Feng^{1,2} | Zhen-Hua Ge^{1,2}

¹Faculty of Material Science and Engineering and National & Local Joint Engineering Laboratory of Advanced Metal Solidification Forming and Equipment Technology, Kunming University of Science and Technology, Kunming, China | ²Southwest United Graduate School, Kunming, China | ³Ernst Ruska-Centre For Microscopy and Spectroscopy with Electrons, Forschungszentrum Jülich GmbH, Jülich, Germany | ⁴Center for Electron Microscopy, South China University of Technology, Guangzhou, China

Correspondence: Lei Jin (l.jin@fz-juelich.de) | Jing Feng (jingfeng@kust.edu.cn) | Zhen-Hua Ge (zge@kust.edu.cn)

Received: 27 October 2025 | **Revised:** 12 December 2025 | **Accepted:** 22 December 2025

Keywords: Bi₂S₃ | FeCoNi doping | porous structures | thermoelectric materials

Bismuth sulfide (Bi₂S₃) exhibits potentials in thermoelectric field, due to their environmental friendliness, high Seebeck coefficients, and low thermal conductivity. However, the peak ZT for binary Bi₂S₃ does not exceed 1.0, inhibiting its practical applications. Starting from the precipitation smelting of bismuth concentrate process, this study constructs multi-type, multi-scale in-situ secondary phases and porous structures through FeCoNi (FCN) medium-entropy alloy addition, significantly enhancing the ZT value of Bi₂S₃-based thermoelectric materials. The introduced FCN reacts with pre-synthesized Bi₂S₃ nanorod matrix during spark plasma sintering and forms precipitate complex with FCN-S core and Bi shell microstructures. FCN doping improves the carrier concentration of Bi₂S₃ and the reduced Bi from Bi₂S₃ acts as carrier transport channels for mobility optimization. Due to the stacking effect of Bi₂S₃ nanorods and the volatile nature of metallic Bi, porous Bi₂S₃ structure is formed, characterized by randomly-distributed and micro-to-nanoscale pores. The coexistence of various lattice defects effectively scatter phonons and suppress the lattice thermal conductivity, thus an excellent peak ZT of 1.1 is achieved at 773 K in a 0.25 wt.% FCN-doped Bi₂S₃ sample. This study, drawing on the process of ore smelting, proposes a convenient method for preparing high-performance chalcogenide thermoelectric materials with porous structures.

1 | Introduction

Thermoelectric materials can directly convert waste heat into electricity using the Seebeck effect or convert electricity into heat using the Peltier effect without moving component parts or generating toxic gases, thus providing a new approach to overcome the increasingly serious environmental issues and energy crisis [1–3]. The performance of a thermoelectric material is evaluated using the dimensionless figure of merit ZT [4–6]. $ZT = (\sigma S^2 / \kappa_{\text{tot}})T$, where σ , S , κ_{tot} , and T represent the electrical conductivity,

the Seebeck coefficient, the total thermal conductivity, and the absolute temperature (in K), respectively.

Simultaneous optimization of the electrical and thermal transport properties is challenging due to the complex and strong coupling among the σ , S , and κ_{tot} parameters. Nevertheless, the power factor ($PF = \sigma S^2$) can be effectively improved by increasing σ using carrier engineering [7–9] (modulation doping and elemental alloying for carrier density optimization) and by increasing S using band-structure engineering [10–12] (enhancing band

This is an open access article under the terms of the [Creative Commons Attribution](https://creativecommons.org/licenses/by/4.0/) License, which permits use, distribution and reproduction in any medium, provided the original work is properly cited.

© 2026 The Author(s). *Advanced Materials* published by Wiley-VCH GmbH

degeneracy and band convergence for effective mass optimization). In parallel, decreasing lattice thermal conductivity (κ_{lat}) is also beneficial for enhancing the ZT value. Strategies have been developed to optimize thermal transport property, such as enhancing the phonon scattering through the introduction of nanostructure precipitates [13–15], utilizing porous structures [16, 17], or seeking new materials with intrinsically low thermal conductivities [18–20].

There are many state-of-the-art thermoelectric materials with excellent thermoelectric performances, such as Bi_2Te_3 [21–24], PbQ-based (Q = S, Se, and Te) [25–28], SnTe-based [11, 29], and Half-Heusler alloys [30, 31]. However, their large-scale applications are still restricted due to the requirement of rare and expensive elements, such as Te, or toxic and carcinogenic elements, such as Pb, Cd, and Sb. As a consequence, it is critical to find and further optimize new candidates that contain earth-abundant and environment-friendly elements in order to boost further market applications. Recently, Pb-free Bi_2S_3 , consisting of abundant, cheap, and low-toxic elements, has attracted increasing attention for medium-temperature commercial applications. Bi_2S_3 has a room-temperature (RT) orthorhombic structure, and the chemical bonds between Bi and S are more ionic than covalent. Because of the significantly large difference in electronegativities of Bi (= 1.9) and S (= 2.58), a strong optical phonon scattering is generated, resulting in a low κ_{lat} and poor carrier mobility [32]. The large S value and a relatively low κ_{lat} make Bi_2S_3 a promising medium-temperature thermoelectric material. However, the low σ seriously inhibits its improved thermoelectric properties, as the intrinsic carrier concentration (n) of Bi_2S_3 is as low as 10^{17} cm^{-3} . Previous studies have demonstrated that metal element doping (such as Ag [33, 34], Cu [35, 36], Ce [37]) can effectively modulate the carrier concentration and phonon scattering in Bi_2S_3 -based thermoelectric materials, thereby enhancing their performance. Meanwhile the hydrothermal method combined with spark plasma sintering (SPS) has also been employed to construct tailored microstructures for further optimization. For instance, Liu et al. [38] synthesized Bi_2S_3 nano-networks via a solution-based approach and achieved a ZT value of 0.5 at 723 K through grain boundary purification. Xu et al. [16] further engineered the stacking of Bi_2S_3 nano-networks and introduced a porous structure via SPS, which significantly reduces κ_{lat} and achieves a peak ZT of 0.81 at 823 K. This highlights the synergistic enhancement of thermoelectric properties through microstructural design.

Introducing porous structures into bulk thermoelectric materials has been theoretically proven to effectively optimize the thermoelectric properties. Various strategies have been proposed to construct porous structures in bulk thermoelectric materials, including assembly of hollow nanostructures [39], chemical exfoliation [40], sublimating agent-assisted pore formation [41], and explosive reaction methods [42]. However, the intense carrier/phonon scattering at the interface between the matrix material and pores may lead to simultaneous reductions in σ and κ_{lat} . Since the decrease in κ_{lat} cannot fully compensate for the deterioration of σ , the ZT value may be eventually reduced. In this regard, designing the interface between the matrix and pores, as well as controlling the size and distribution of pores, is crucial for the performance improvements of thermoelectric materials.

In this work, hydrochloric acid-pretreated Bi_2S_3 nanorods are mixed with iron-based medium-entropy alloy (FeCoNi, abbreviated as FCN) and Bi_2S_3 -based bulk polycrystalline materials are synthesized by SPS following the precipitation melting process [43]. The synthetic details are shown in Figure S1. In the precipitation melting process, FCN could react with Bi_2S_3 concentrate, generating metallic Bi and $(\text{Fe,Co,Ni})\text{S}_x$ (FCN-S) precipitates; meanwhile, FCN can also enter Bi_2S_3 lattice and achieve effective doping, as shown in Figure 1a. The reduced Bi forms around the FCN-S compounds, resulting in a nested distribution of the multiple and multiscale precipitates. The n and the carrier mobility (μ) of Bi_2S_3 material are simultaneously improved due to the heterovalent FCN doping and the formation of conductive channels through the reduced Bi precipitates. Therefore, the highly enhanced σ and PF is realized (Figure 1b,c). Moreover, densely distributed and multi-scale pores are formed (Figure 1a), which are induced by nanorod stacking and volatilization of the reduced Bi metals (under the high temperature (HT), high pressure (HP) and vacuum environmental conditions during SPS). The complex microstructures, consisting of metal sulfides and multi-scale pores, could effectively scatter phonons with different frequencies, leading to an ultralow κ_{lat} (Figure 1d). Ultimately, an n-type, binary, polycrystalline $\text{Bi}_2\text{S}_3 + 0.25 \text{ wt.}\%$ FCN sample is obtained with an excellent ZT value of 1.1 at 773 K (Figure 1e), surpassing previous reports and demonstrating the potential of Bi_2S_3 materials for thermoelectric applications in the middle-temperature region.

2 | Results and Discussion

The X-ray diffraction (XRD) patterns of the bulk $\text{Bi}_2\text{S}_3 + x \text{ wt.}\%$ FCN ($x = 0, 0.125, 0.25, 0.5, 1.0$) samples are shown in Figure 2a. All featured peaks match well with the orthorhombic Bi_2S_3 phase. The enlarged XRD pattern for the diffraction angle between $24\text{--}26^\circ$ is shown in Figure 2b. As x increases, the XRD peaks gradually shift toward lower angles, suggesting a systematic lattice expansion of the Bi_2S_3 matrix. The lattice expansion may be explained by the fact that the FCN ions enter the interstitial sites of Bi_2S_3 . Volatilization of S during SPS may be another reason for the volume increase, as reported in literature [44]. Notably, the diffraction peaks corresponding to metallic Bi can be detected when the FCN content reaches 1.0 wt.%. Furthermore, the elemental Bi is further verified using differential scanning calorimetry for all samples in the 300 – 800 K temperature range, and the results are shown in Figure 2c. The $\text{Bi}_2\text{S}_3 + 1.0 \text{ wt.}\%$ FCN sample shows an obvious absorption peak near 542.5 K, consistent with the melting point of metallic Bi at 544.4 K. Additionally, the thermogravimetry curves do not show a decreasing inflection point in the measured temperature range, indicating a good thermal stability of the prepared Bi_2S_3 samples, as shown in Figure S2.

As shown in Figure 3a, the chemical state of different elements on the surface of the as-synthesized bulk samples is analyzed using X-ray photoelectron spectroscopy (XPS). Here, $\text{Bi}_2\text{S}_3 + 0.25 \text{ wt.}\%$ FCN is used as a typical example. As shown in Figure 3b, the peak at 441.2 eV corresponds to Bi $4d_{5/2}$ of the Bi metal [45], indicating the presence of Bi metal in this sample. Apparently, the amount is beyond the detection limit of XRD and DSC. The peaks at 158.1 and 163.4 eV can be attributed to the Bi $4f_{7/2}$ and Bi $4f_{5/2}$ orbits,

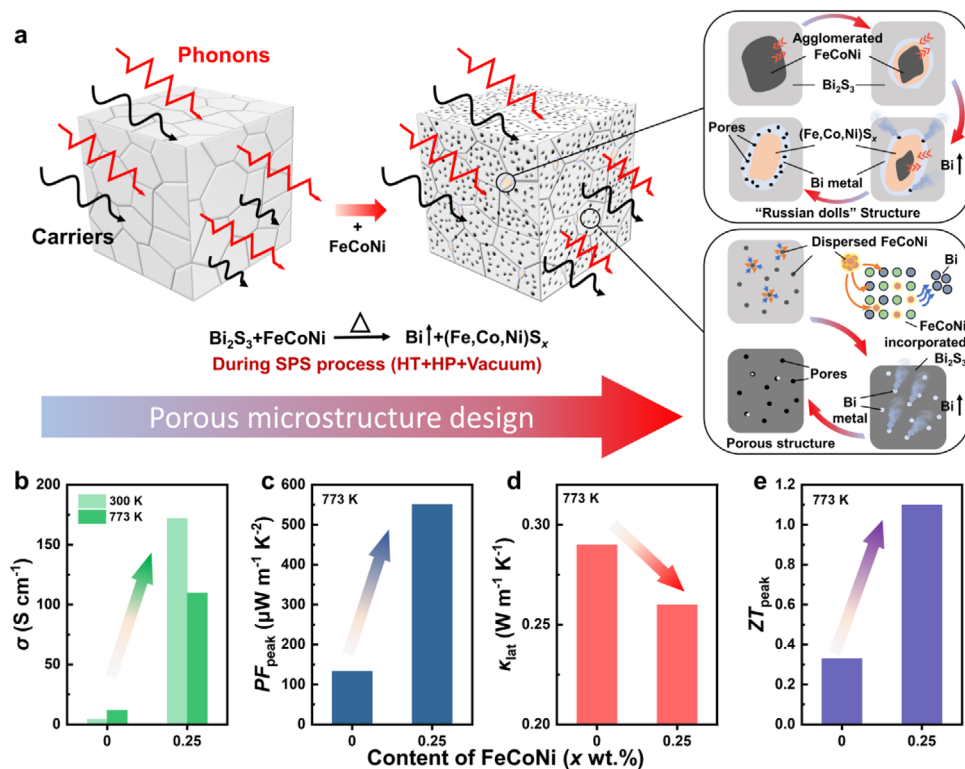


FIGURE 1 | Schematic diagram of the Bi_2S_3 based bulk material with complex microstructure prepared by SPS of Bi_2S_3 nanorods and FeCoNi alloy nano-powders. (a) The formation process of the porous structure. (b) Electrical conductivity, (c) peak power factor, (d) lattice thermal conductivity and (e) ZT of Bi_2S_3 and $\text{Bi}_2\text{S}_3 + 0.25$ wt.% FCN bulk samples.

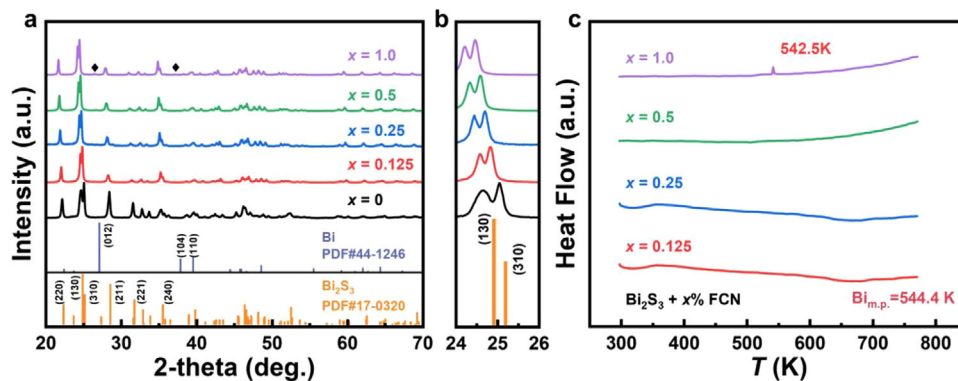


FIGURE 2 | (a) XRD patterns and (b) expanded plots for the (130) and (310) peaks of $\text{Bi}_2\text{S}_3 + x$ wt.% FCN ($x = 0, 0.125, 0.25, 0.5, 1.0$). (c) Differential scanning calorimeter results for all samples in the range of 300 – 800 K.

respectively [46]. Additionally, as shown in Figure 3c, two minor peaks are detected at 160.8 and 162.0 eV in the same band area of the Bi 4f orbit, arising from S $2p_{3/2}$ and S $2p_{1/2}$ [47]. Consequently, the valence state of the matrix elements Bi and S are +3 and -2, respectively. In comparison with Bi and S, Fe, Co and Ni have weaker peak intensities, indicating that their contents are low on the measured surface. As shown in Figure 3d, the Fe^{3+} species are present, and the binding energies at 711.8 and 724.9 eV can be ascribed to $\text{Fe}^{3+} 2p_{3/2}$ and $\text{Fe}^{3+} 2p_{1/2}$ [48], respectively. Additionally, the peak with binding energy at 715.7 eV can be attributed to the satellite peak of Fe 2p. As shown in the Co 2p spectrum in Figure 3e, the main doublets at 781.8, 796.7, 780.3, and 795.2 eV correspond to $\text{Co}^{2+} 2p_{3/2}$, $\text{Co}^{2+} 2p_{1/2}$, $\text{Co}^{3+} 2p_{3/2}$, and

$\text{Co}^{3+} 2p_{1/2}$, respectively [48]. As shown in the Ni 2p spectrum in Figure 3f, Ni^{2+} (854.3 for $\text{Ni}^{2+} 2p_{3/2}$ and 872.1 eV for $\text{Ni}^{2+} 2p_{1/2}$) and Ni^{3+} (856.3 for $\text{Ni}^{3+} 2p_{3/2}$ and 874.1 eV for $\text{Ni}^{3+} 2p_{1/2}$) coexist [49, 50]. Notably, the Fe, Co, and Ni metallic states cannot be detected in the $\text{Bi}_2\text{S}_3 + x$ wt.% FCN sample, indicating that FCN reacts with the Bi_2S_3 matrix during SPS and forms compounds.

The backscattered electron (BSE) scanning electron microscopy (SEM) image shown in Figure 4a reveals three different contrasts (i.e., grey, black and white) in the $\text{Bi}_2\text{S}_3 + 0.25$ wt.% FCN sample. Same contrasts are also observed in other FCN treated samples, as shown in Figure S3. The elemental distribution results obtained by electron probe micro analysis (EMPA) reveal that the gray

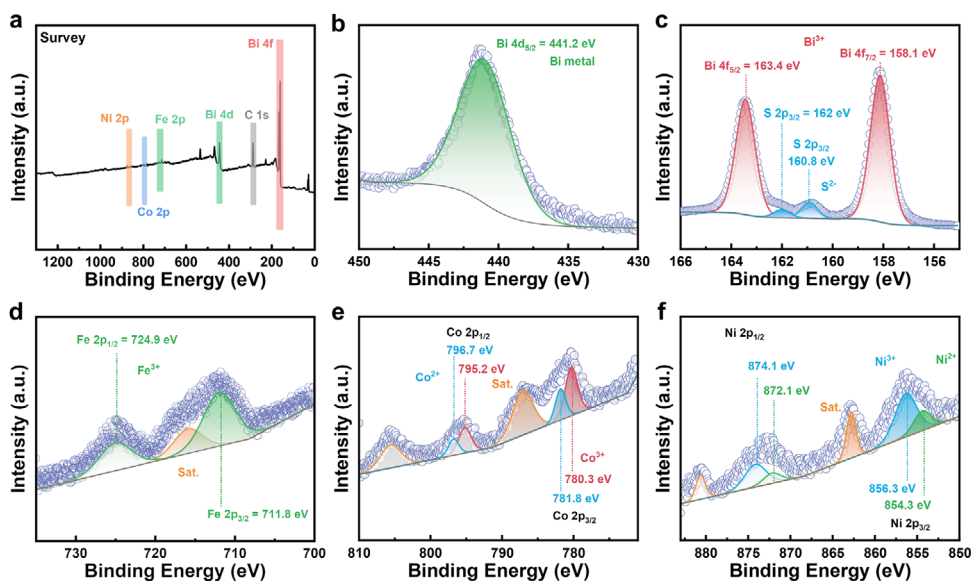


FIGURE 3 | High resolution XPS spectra of the $\text{Bi}_2\text{S}_3 + 0.25 \text{ wt.}\%$ FCN sample. (a) Survey spectrum and spectra of (b) Bi 4d, (c) Bi 4f and S 2p, (d) Fe 2p, (e) Co 2p and (f) Ni 2p.

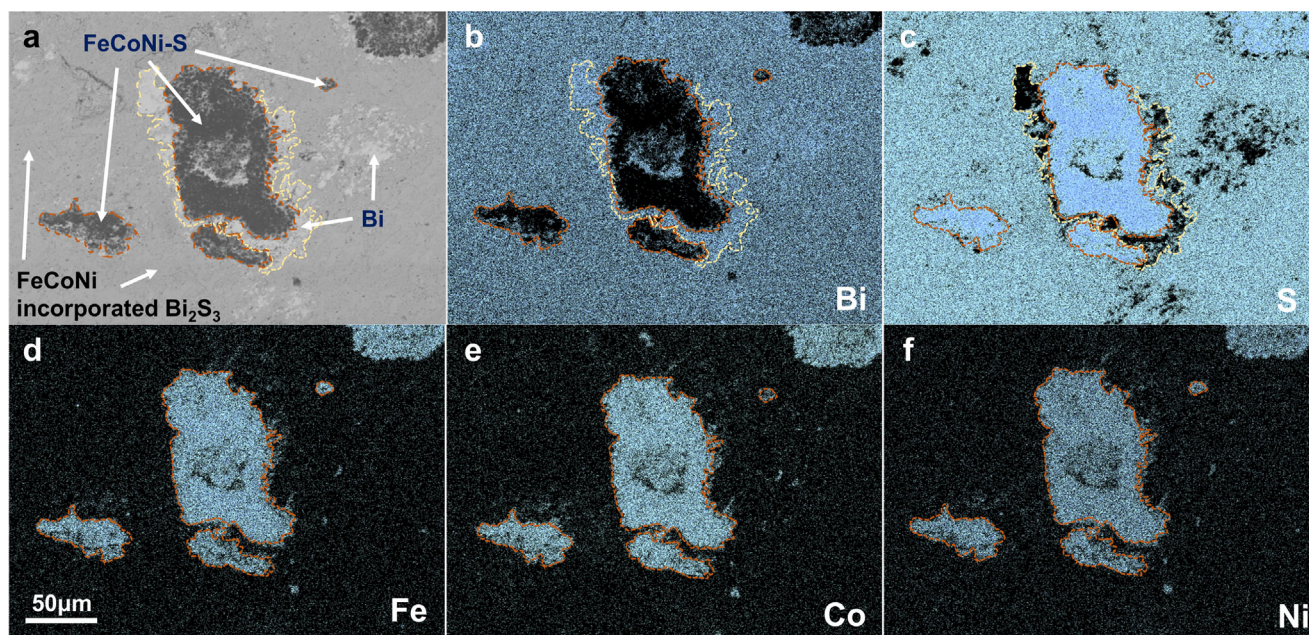


FIGURE 4 | (a) BSE SEM image of the $\text{Bi}_2\text{S}_3 + 0.25 \text{ wt.}\%$ FCN sample. The sample surface is polished for measurements. EPMA elemental mapping result of (b) Bi, (c) S, (d) Fe, (e) Co and (f) Ni element in the $\text{Bi}_2\text{S}_3 + 0.25 \text{ wt.}\%$ FCN sample. The results are obtained from identical locations, therefore a global scale bar is displayed in (d).

area is the Bi_2S_3 matrix incorporated by a small amount of Fe, Co and Ni (denote FCN incorporated Bi_2S_3 , see also Figure S4 and Table S1). The distribution of Fe, Co and Ni is found to be uniform, which is beneficial to the overall material conductivity. The black area is primarily enriched with Fe, Co, Ni and S elements, indicating the formation of FCN-S compounds. This is consistent with the XPS results. The density of this FCN-S phase increases as the FCN content is increased, as evidenced in Figure S3. The white region is metallic Bi, which is formed as a result of the reduction reaction between FCN and Bi_2S_3 . Notably, the

polymorphic secondary phases form a multilayer “Russian dolls” structure, usually with metal sulfide as the core and metallic Bi as the surrounding layer. Their size can be varied from several to hundreds of microns, which imposes difficulties for scanning transmission electron microscopy (STEM) investigations. Nevertheless, a small-scale “Russian doll” structure is captured in Figure S5 and the energy dispersive X-ray spectroscopy (EDS) results are consistent with EPMA. Such complex microstructures introduce additional phase boundaries, which is expected to reduce κ_{lat} .

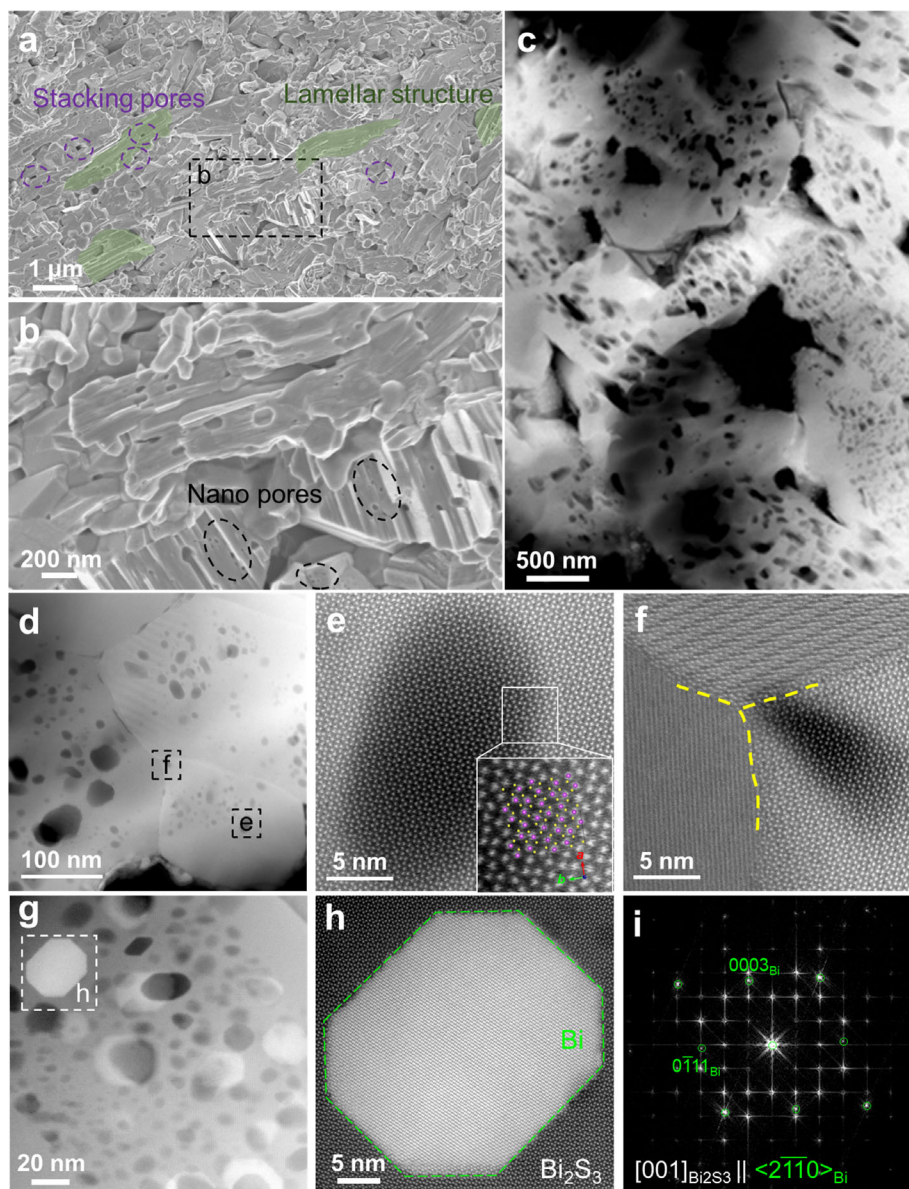


FIGURE 5 | (a) SEM of $\text{Bi}_2\text{S}_3 + 0.25 \text{ wt.}\%$ FCN sample showing the formation of lamellar structure accompanied by the stacking related pores. (b) Magnified SEM from the marked area in (a) showing the presence of nanopores in grains. (c) and (d) High-angle annular dark-field scanning transmission electron microscopy (HAADF-STEM) images of $\text{Bi}_2\text{S}_3 + 0.25 \text{ wt.}\%$ FCN sample at different magnifications. (e) and (f) Atomic-resolution HAADF images of the areas marked in (d). (g) Low magnification HAADF image showing the coexistence of residual Bi and nanopores; (h) Magnified HAADF image of the area marked in (g) and (i) the corresponding fast Fourier transform showing the relationship between Bi and the grain matrix.

The fracture surface morphologies of the $\text{Bi}_2\text{S}_3 + x \text{ wt.}\%$ FCN samples are studied using SEM, as shown in Figure 5a,b and Figure S6. It is evidenced that FCN treatment significantly affects the microstructures, as compared with that of the Bi_2S_3 pure sample shown in Figure S7. On the one hand, the nanorod morphology is reduced with increased FCN treatment. We note that FCN has a high electrical conductivity ($7000 - 8000 \text{ S cm}^{-1}$) [51], it increases the local current density during SPS. This creates HT spots and leads to local overheating, thus reshaping the grain morphology. On the other hand, the average Bi_2S_3 grain size decreases from 600 to 400 nm as FCN content increases from 0.125 to 1.0 wt.%, as shown in Figure S6. This can be interpreted by the fact that the increase in FCN content increases the HT spots. In addition, the presence of hard secondary phases (FCN-

S) may also hinder the grain growth during sintering. With the abovementioned reasons, a typical laminar structure is formed and accompanying the nanorod stacking, pores are also evident, as shown in Figure 5a. The size of these stacking related pores is measured for the pure and $x = 0.25$ samples, as shown in Figure S8. With FCN reaction, the size is reduced suggesting a better grain connectivity and structural densification. This is evidenced by the increase of relative densities as a function of x , measured by Archimedes method (Table S2).

The reaction of FCN not only introduces multi-scale “Russian dolls” structure into the matrix, but also leads to the formation of abundant nanoporosity within the matrix grains, creating a nanoporous structure. Unlike the stacking induced pores (with

larger pore size), these nanopores are less than 50 nm as evidenced by the magnified SEM image shown Figure 5b. In order to further understand the microstructures, we perform STEM together with EDS.

Figure 5c,d shows the low-magnification high-angle annular dark-field (HAADF) STEM images (so-called Z-contrast images, Z: atomic number) of the $\text{Bi}_2\text{S}_3 + 0.25$ wt.% FCN sample and densely distributed nanoscale pores can be observed in the matrix grains, consistent with the SEM observations. In order to minimize the influence from STEM sample preparation, we also prepared ground particles (dispersed on holy carbon grids), which exhibit the same nano-porous structure, as shown in Figure S9. Statistical measurement reveals that the average size of pores is about 30 nm (Figure S9). The EDS result from the area in Figure 5d (see Figure S10) shows that the Fe, Co and Ni are distributed uniformly in the matrix (i.e., FCN incorporated Bi_2S_3), which is consistent with the EMPA result.

Two areas marked by the dashed frames are further magnified as Figure 5e,f. In Figure 5e, atomic resolution is obtained along the c-axis and the atomic details match well with the superimposed Bi_2S_3 structure (Bi: purple and S: yellow). Except the contrast difference in this image, no other changes are detected, suggesting that the dark contrast area is indeed a nanopore. In Figure 5f, a grain boundary triple junction is revealed. It is seen that the boundaries maintain atomic-layer contacts and no amorphous regions are present.

Nanosized Bi metals are also found inside the grains (Figure 5g), which show an orientation relationship of $\langle 2\bar{1}10 \rangle_{\text{Bi}} \parallel [001]_{\text{Bi}_2\text{S}_3}$ with the matrix (Figure 5h,i; Figure S11). They usually coexist with nanopores, as shown in Figure 5g; Figure S9 and Figure S11, indicating that the formation of nanosized Bi and nanopores is actually correlated. The most likely mechanism is discussed as follows (see also Figure 1a for demonstration): First, during SPS, small/dispersed FCN particles react with matrix and FCN incorporation to the Bi_2S_3 lattice (including replacement of Bi and interstitial site filling) therefore occurs. This leads to the lattice expansion of the FCN incorporated Bi_2S_3 , as supported by Figure 2, Figure 4 and Figure S10. Second, as a result of replacement, metallic Bi is reduced from the lattice and forms nanosized particles. Since SPS is in a HT, HP and vacuum environment, most of the metallic Bi nanoparticles volatilized (due to the size effect, the smaller the size, the lower the evaporation temperature [52–54]), leaving densely distributed nanopores together with residual Bi nanoparticles in the grain matrix (e.g., Figure 5g).

For the $\text{Bi}_2\text{S}_3 + x$ wt.% FCN bulk samples, σ as a function of T is shown in Figure 6a. Compared with pure Bi_2S_3 , the σ value is significantly higher for the $\text{Bi}_2\text{S}_3 + x$ wt.% FCN samples over the full temperature range. As x increases, σ increases continuously. At 300 K, it increases from 4 S cm^{-1} for the pure Bi_2S_3 sample to 327 S cm^{-1} for the $x = 1.0$ sample, an increase of two orders of magnitude. In addition, σ of the FCN treated samples decreases gradually with the increased T , indicating that the conductive characteristics changes from that of a semiconductor to a degenerate semiconductor. All of these results indicate that (at least part of) FCN enters the Bi_2S_3 lattice and achieves effective doping. This is consistent with the XPS and EDS results.

The plots of S versus T for the $\text{Bi}_2\text{S}_3 + x$ wt.% FCN samples are shown in Figure 6b. All of the samples show negative S values, indicating that they are n-type semiconductors. Thus, electrons are the main carriers. Opposite to the σ case, the S values decrease as x increases. Figure 6c plots the Pisarenko curves, which demonstrate the relationship between carrier concentration n_e (subscript e denotes electrons), S and the effective mass of the carriers (m^*) [55]. It is evident that at 300 K, m^* decreases gradually as x increases. In combination with the result in Figure 7a, it is found that the decrease in $|S|$ as x increases is a combined effect from increased n_e and decreased m^* . Particularly, the $|S|$ value of the $x = 0.25$ sample increases from 128 at 300 K to 224 $\mu\text{V K}^{-1}$ at 773 K, meaning that a good S value is maintained over the measured temperature range. Figure 6d plots the PF values as a function of T , which will be discussed later.

Furthermore, the effect of FCN on the electrical transport properties is studied using variable-temperature Hall measurements. Figure 7a plots n_e as a function of T for the $\text{Bi}_2\text{S}_3 + x$ wt.% FCN ($x = 0, 0.125, 0.25, 0.5,$ and 1.0) samples. The n_e value of pure Bi_2S_3 increases with T , primarily due to the thermal excitation of carriers. The FCN incorporated samples have n_e with negligible T -dependence. Additionally, n_e increases with x due to the enhanced incorporation of FCN to the Bi_2S_3 matrix during sintering. The n_e values are 9.05×10^{17} and $2.84 \times 10^{19} \text{ cm}^{-3}$ for pure Bi_2S_3 and the $\text{Bi}_2\text{S}_3 + 1.0$ wt.% FCN sample, respectively. Figure 7b shows the variation of the carrier mobility μ_H as a function of T for the $\text{Bi}_2\text{S}_3 + x$ wt.% FCN ($x = 0, 0.125, 0.25, 0.5,$ and 1.0) samples. For all of the samples, μ_H decreases with increased T and the decreasing trend matches the $T^{-3/2}$ law, indicating that the scattering mechanism is primarily phonon scattering. Meanwhile, the μ_H values increases significantly as x increases. At RT, the μ_H values for the $x = 0.125$ and 1.0 samples are 43 and 72 $\text{cm}^2 \text{ V}^{-1} \text{ s}^{-1}$, respectively. Such a significant increase in the carrier mobility can be understood from the following aspects: First, the reduction of Bi_2S_3 by FCN during sintering creates metallic Bi, which can act as a grain lubricant and sintering aid. This not only promotes the alignment of nanorods under pressure, but more importantly decreases the stacking induced pores that sever macroscopic conduction paths. Although the newly formed nanopores act as scattering centers, their detrimental impact is far outweighed by the repair of conductive paths resulting from elimination of stacking induced pores. Second, the precipitated Bi metal serves as a bridge for the fast migration of carriers. Third, the FCN-S phases as a result of FCN and Bi_2S_3 reaction usually have excellent σ , which have been widely used in energy conversion and storage (e.g., electrocatalysis [56, 57] and supercapacitors [58, 59]).

Now the weighted mobility (μ_w) is calculated using the following formula to better evaluate the intrinsic electrical transport properties of the $\text{Bi}_2\text{S}_3 + x$ wt.% FCN samples [60]:

$$\mu_w = \frac{3h^3\sigma}{8\pi(2m_e kBT)^{\frac{3}{2}}} \times \left[\frac{\exp\left[\frac{|S|}{k_B/e} - 2\right]}{1 + \exp\left[-5\left(\frac{|S|}{k_B/e} - 1\right)\right]} + \frac{\frac{3}{\pi^2} \frac{|S|}{k_B/e}}{1 + \exp\left[5\left(\frac{|S|}{k_B/e} - 1\right)\right]} \right]$$

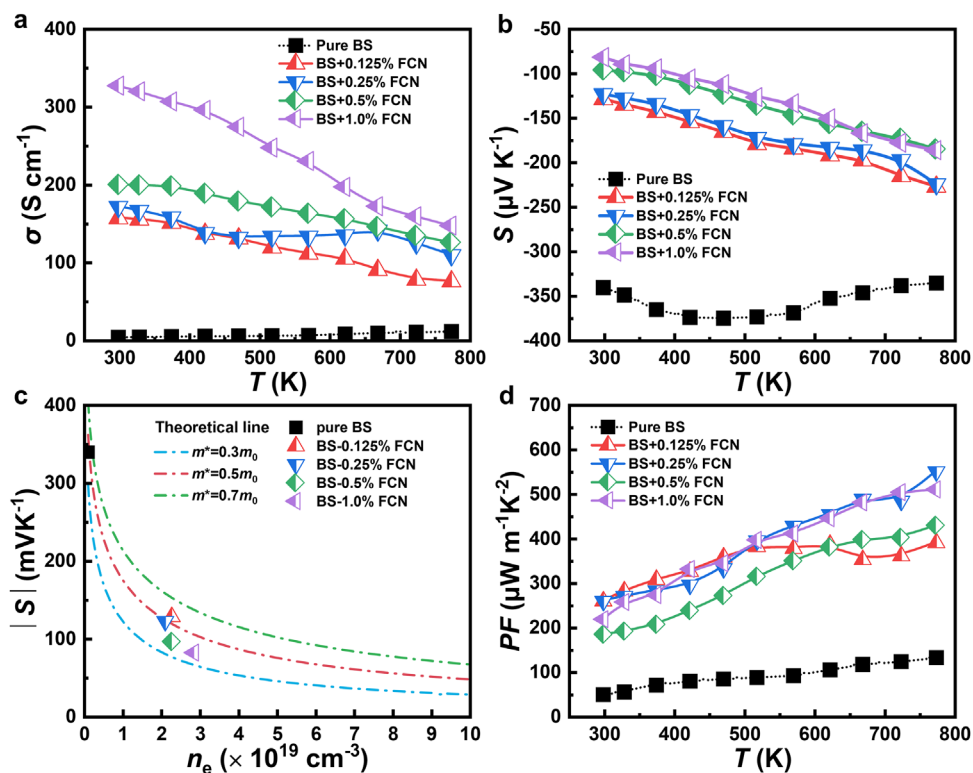


FIGURE 6 | Electrical transport properties of Bi₂S₃ + x wt.% FCN (x = 0, 0.125, 0.25, 0.5, 1.0). (a) σ ; (b) S ; (c) Pisarenko curves and (d) PF . BS represents Bi₂S₃ for short.

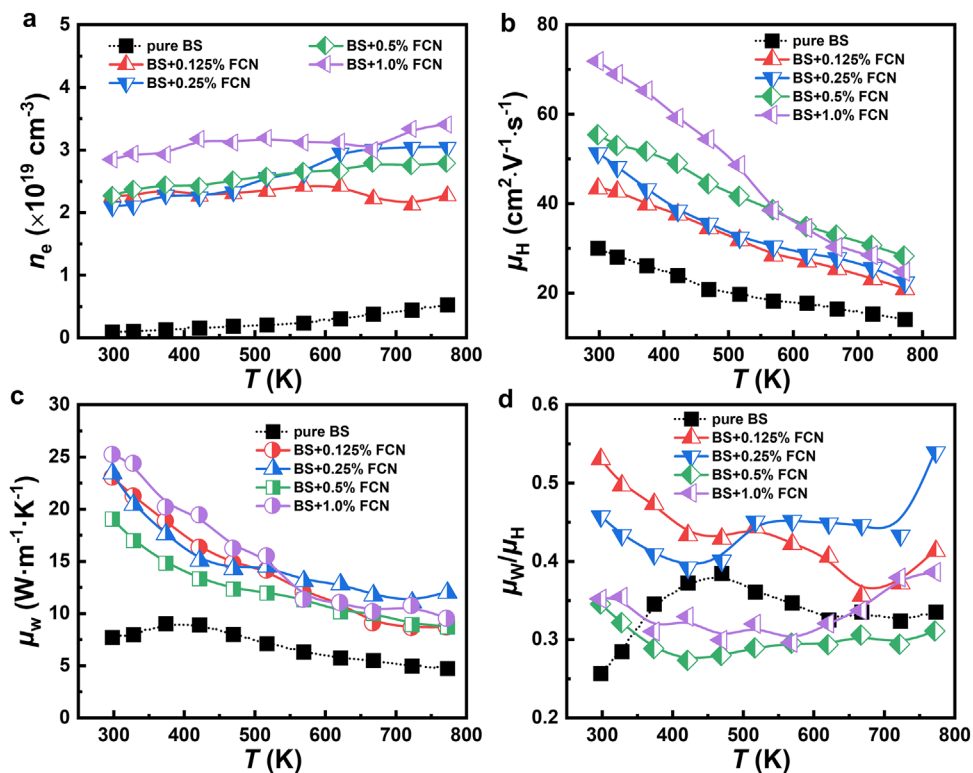


FIGURE 7 | Temperature-dependent (a) carrier concentration; (b) Hall carrier mobility; (c) weighted mobility, and (d) the ratio of weighted mobility to carrier mobility for Bi₂S₃-x wt.% FCN (x = 0, 0.125, 0.25, 0.5, 1.0) samples. BS represents Bi₂S₃ for short.

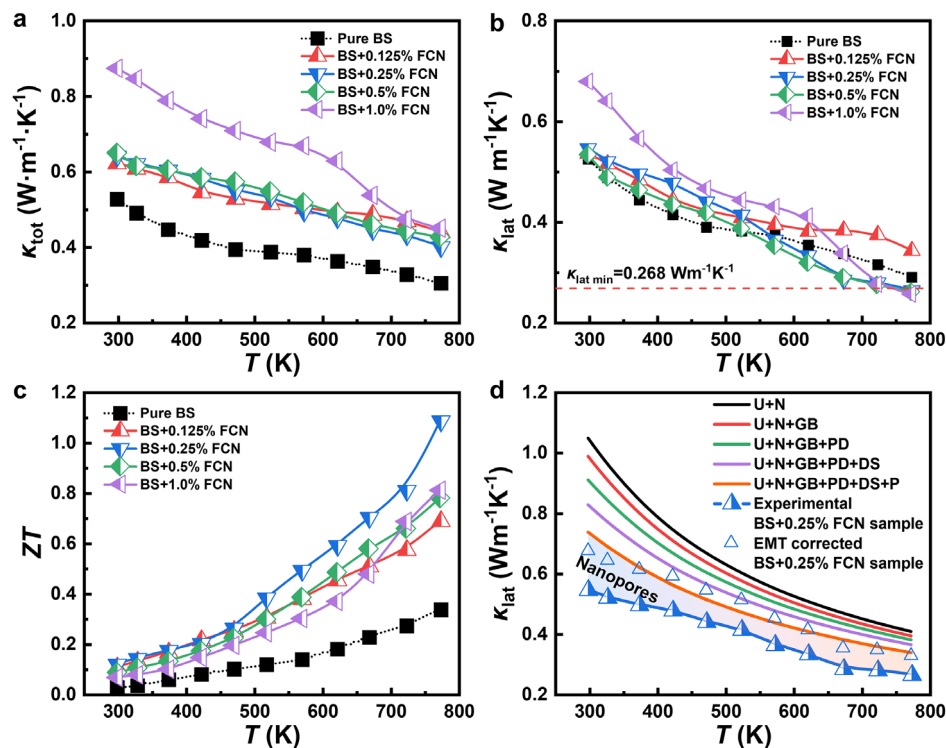


FIGURE 8 | Thermal transport properties of Bi₂S₃-x wt.% FCN ($x = 0, 0.125, 0.25, 0.5, 1.0$). (a) Total thermal conductivity, (b) lattice thermal conductivity and (c) ZT values. (d) Contribution of different phonon mechanisms calculated by the Debye-Callaway theory showing the influence of nanopores on κ_{lat} of the Bi₂S₃ + 0.25 wt.% FCN sample (Cf. text for details). BS represents Bi₂S₃ for short.

where, k_B , h , m_e and e represent the Boltzmann constant, Planck constant, electron mass, and electron charge, respectively. As demonstrated in Figure 7c, the FCN incorporated samples show enhanced μ_W values than pure Bi₂S₃, manifesting improved electrical transport properties. In addition, the ratio between μ_W and μ_H (i.e., μ_W/μ_H) (Figure 7d) could study the change in m^* according to the following formula [55]:

$$\mu_W \approx \mu_H \left(\frac{m^*}{m_e} \right)^{\frac{3}{2}}$$

At RT, μ_W/μ_H decreases as x increases, which is consistent with the change in m^* , as demonstrated in Figure 6c. After 600 K, the $x = 1.0$ sample shows a significantly increased μ_W/μ_H value than the $x = 0.5$ sample. This explains why the former has higher S value than that of the latter after 600 K.

Now we return to Figure 6d, the FCN incorporated samples exhibit significantly enhanced PF than pure Bi₂S₃. The Bi₂S₃ + 0.25 wt.% FCN sample has the highest PF of 551 $\mu\text{W m}^{-1} \text{K}^{-2}$ at 773 K. FCN not only optimizes n_e but also increase μ_H . The increased σ coupled with a large S value significantly enhances PF over a wide temperature range, suggesting that FCN can improve the electrical transport properties of polycrystalline Bi₂S₃ over a wide temperature range, thus resulting in a high average ZT value. Moreover, repeatability test of σ and S (Figure S12) and the vacuum annealing results (Figure S13) demonstrate excellent thermal stability of the material.

The thermal transport properties of Bi₂S₃ + x wt.% FCN ($x = 0, 0.125, 0.25, 0.5, 1.0$) samples are studied in Figure 8.

In Figure 8a, the κ_{tot} of the samples increases with the FCN content, suggesting a deteriorated contribution in the thermoelectric performance. The κ_{tot} values of pure Bi₂S₃ and the $x = 1.0$ sample are 0.52 and 0.87 $\text{W m}^{-1} \text{K}^{-1}$ at RT, respectively. Nevertheless, considering the great improvement in the electrical properties, such deterioration in thermal transport is mild. Note that κ_{tot} consists of two components: κ_{lat} and electronic thermal conductivity (κ_{ele}). The latter can be calculated using $\kappa_{\text{ele}} = L\sigma T$, where L represents the Lorentz number and can be calculated by assuming the single parabolic band model (SPB) and by fitting the measured S values [61]. Specifically, acoustic phonon scattering is assumed as the dominant scattering mechanism (scattering factor $r = -1/2$) for the SPB model calculations, which is supported by the observed $\mu_H \propto T^{-3/2}$ relationship shown in Figure 7b. Plots of κ_{lat} ($= \kappa_{\text{tot}} - \kappa_{\text{ele}}$) and κ_{ele} are presented in Figure 8b and Figure S14, respectively, as a function of T for all samples. This allows the individual contribution from κ_{lat} and κ_{ele} to be evaluated. It is evidenced that the increase in κ_{tot} is mainly from the κ_{ele} contribution. This is predictable as the increased n_e caused by FCN incorporation inevitably increases κ_{ele} . In contrast, the rise of κ_{lat} of the FCN treated samples is not significant. Notably, κ_{lat} becomes even lower than the pure case when $T > 550$ K for the $x = 0.25$ and 0.5 samples. At 773 K, the values are 0.27 and 0.26 $\text{W m}^{-1} \text{K}^{-1}$, respectively, reaching the amorphous limiting value of $\sim 0.27 \text{ W m}^{-1} \text{K}^{-1}$ for Bi₂S₃ based on the Cahill model [62, 63]. By combining results in Figure 6d and Figure 8a, the ZT values are plotted in Figure 8c. It is seen that the electrical and thermal properties reach the best compromise for the $x = 0.25$ sample across the entire temperature range and a peak ZT of 1.1 is achieved at 773 K, which is almost three times that of pure Bi₂S₃.

From the microstructure results, the following issues can be discussed to understand the variation of κ_{lat} . First, metallic Bi has a high thermal conductivity, thereby, the residual Bi in the FCN treated samples should increase κ_{lat} with reference to the pure sample at low temperatures. When the temperature exceeds 544.3 K (i.e., melting point of Bi), the residual Bi becomes liquid, thus decreasing κ_{lat} at high temperatures. Second, the reduced size of stacking related pores and the improved grain connectivity in the FCN treated samples should increase κ_{lat} . Third, densely distributed nanopores are reported to be effective source for phonon scattering. In this regard, their presence should decrease κ_{lat} over a wide temperature range.

To further understand the phonon scattering mechanisms, Debye–Callaway model is used to analyze κ_{lat} of the $\text{Bi}_2\text{S}_3 + 0.25 \text{ wt.}\%$ FCN sample using the following equation [64, 65]:

$$\kappa_{\text{lat}} = \frac{k_{\text{B}}}{2\pi^2v} \left(\frac{k_{\text{B}}T}{\hbar} \right)^3 \int_0^{\theta_{\text{D}}} \tau_{\text{c}} \frac{\chi^4 e^{\chi}}{(e^{\chi} - 1)^2} d\chi$$

where \hbar , v , θ_{D} , χ and τ_{c} represent Planck's reduced constant, average sound velocity, Debye temperature, reduced phonon frequency (defined as $\hbar\omega/k_{\text{B}}T$, where ω is the phonon angular frequency) and total phonon relaxation time, respectively. τ_{c} can be expressed using the following equation:

$$\frac{1}{\tau_{\text{c}}} = \frac{1}{\tau_{\text{U}}} + \frac{1}{\tau_{\text{N}}} + \frac{1}{\tau_{\text{GB}}} + \frac{1}{\tau_{\text{PD}}} + \frac{1}{\tau_{\text{DS}}} + \frac{1}{\tau_{\text{P}}}$$

where, τ_{U} , τ_{N} , τ_{GB} , τ_{PD} , τ_{DS} and τ_{P} represent the relaxation times corresponding to the scattering from the phonon-phonon U-process (U), phonon-phonon N-process (N), grain/phase boundaries (GB), vacancies/alloy elements (point defects, abbreviated as PD), dislocations (DS), and precipitates (P, mainly related to the FCN-S and remained Bi second phases), respectively. As seen from Figure 8d, the fitted κ_{lat} values using the Debye–Callaway model (see Table S3, for details) deviate from the experimental results, even when the influence from the known defects with different scales on phonon relaxation time has been fully considered. It is therefore reasonable to deduce that the mismatch between experimental and fitted values are caused by nanopores. Typically, point defects scatter high-frequency phonons, while grain boundaries and micropores target low-frequency ones. However, mid-frequency phonons often lack effective scattering mechanisms. The appropriate size of nanopores effectively bridges this gap in the phonon scattering spectrum. Consequently, this multi-scale defect structure ensures efficient broadband phonon scattering, thereby minimizing the lattice thermal conductivity. Effective medium theory [41] (EMT, $\kappa_{\text{L,d}} = \kappa_{\text{L,p}}/(1 - 3\varepsilon/2)$, where $\kappa_{\text{L,d}}$, $\kappa_{\text{L,p}}$ represent the lattice thermal conductivity of dense and porous materials and ε denotes porosity, respectively) is applied to obtain the corrected $\kappa_{\text{L,d}}$ of the dense $\text{Bi}_2\text{S}_3 + 0.25 \text{ wt.}\%$ FCN sample. It can be seen that the values after EMT correction are close to the fitted ones, demonstrating that the nanoporous structures do have an optimizing effect (i.e., ~20% reduction) on κ_{lat} . Similar findings have also been reported in literature [39, 41, 66].

Our results are compared with the reported values in literature, some of the key parameters are displayed in Figure 9. Figure 9a shows the RT μ_{H} values as a function of n_{e} . Notably, the FCN introduction strategy implemented in this study yields a μ_{H}

value superior to those of other doped Bi_2S_3 -based materials, such as Bi_2S_3 doped with SbCl_3 [67], CuBr_2 [68], PbBr_2 [69], $\text{Cu-0.175 mol}\%$ BiCl_3 [70], $0.5 \text{ mol}\%$ $\text{BiCl}_3\text{-Cu}$ [71], and others [32, 37, 72–74]. This observation corroborates the premise that the introduction of FCN could maintain a commendable μ_{H} while increasing n_{e} . Figure 9b summarizes the relationships between μ_{H} and $1/\kappa_{\text{lat}}$ for the $x = 0.25$ sample and other excellent Bi_2S_3 -based materials at 300 K [32, 37, 67–75], which highlights the superior balance in electronic and thermal transport properties due to the introduction of FCN in this study. The FCN-treated sample with values located at the upper right corner exhibits a more desirable combination of high μ_{H} and low κ_{lat} than other Bi_2S_3 -based materials. Figure 9c further compares the T dependent κ_{lat} values between the $x = 0.25$ sample and other reported systems [32, 37, 38, 67–69, 75, 76]. It is obvious that our result is among the best. This is benefited from the present engineering strategy that introduces microstructures covering very broad dimensions, including interfaces (~1 nm), pores (~30 nm), residual Bi (nm to μm), FCN-S (several to hundreds of micrometers).

We also compare ZT , in particular the peak values [32, 37, 38, 67–69, 75–78] (Figure 9d) and the average values (i.e., ZT_{avg} [32, 35, 38, 62, 67, 68, 70–73, 79–87]) over the temperature range of 323 – 673 and 323 – 773 K (Figure 9e). It can be seen that the widely used strategy by employing metal dopants to Bi_2S_3 does not achieve excellent ZT value (usually < 1.0). Instead, by introducing FCN treatment, a record-high peak ZT of 1.1 is achieved at 773 K in this work. In addition to the peak ZT , the ZT_{avg} value can be also improved. Although the value of 0.36 in the 323 – 673 K range is slightly lower than that of the Cu-BiCl_3 co-doped sample [71], the ZT_{avg} in the 323 – 773 K range demonstrates the best performance of about 0.47 among the reported Bi_2S_3 -based materials.

The mechanical properties are important for device application. Here, the mechanical properties of the $\text{Bi}_2\text{S}_3 + x \text{ wt.}\%$ FCN ($x = 0, 0.125, 0.25, 0.5, \text{ and } 1.0$) samples are investigated using nanoindentation with the load force set at 20 mN. Figure 10 shows the two-dimensional (2D) contour plots of the hardness and Young's modulus for the pure and $x = 0.25$ samples. In both samples, the hardness and Young's modulus show position related variations, as evidenced by the color mapping fluctuations. However, the average values for both parameters are significantly improved in the FCN treated sample. Specifically, the hardness increases from 0.76 to 1.18 GPa and the Young's modulus from 19.8 to 30.8 GPa, which are about 55% enhancement. In addition, we find that increasing FCN enhances the mechanical properties, as shown in Figures S15 and S16.

Last but not least, the same strategy has been applied to other chalcogenide thermoelectric systems, including PbS and SnS, and the results are given in Figures S17 and S18, respectively. After adding 1 wt.% FCN, diffraction peaks of Pb are observed in XRD, confirming FCN's capability in reducing Pb. The fracture surface morphology images show increased pore density in the FCN treated sample with reference to the pure PbS. As for SnS, although we don't observe clear Sn diffraction peaks in the $\text{SnS} + x \text{ wt.}\%$ FCN ($x = 0, 1$) sample, the grains in the treated sample become more rounded in comparison with the pure sample and the gaps between grains also increase. All of the results indicate that FCN can be used as a universal modifier for chalcogenide

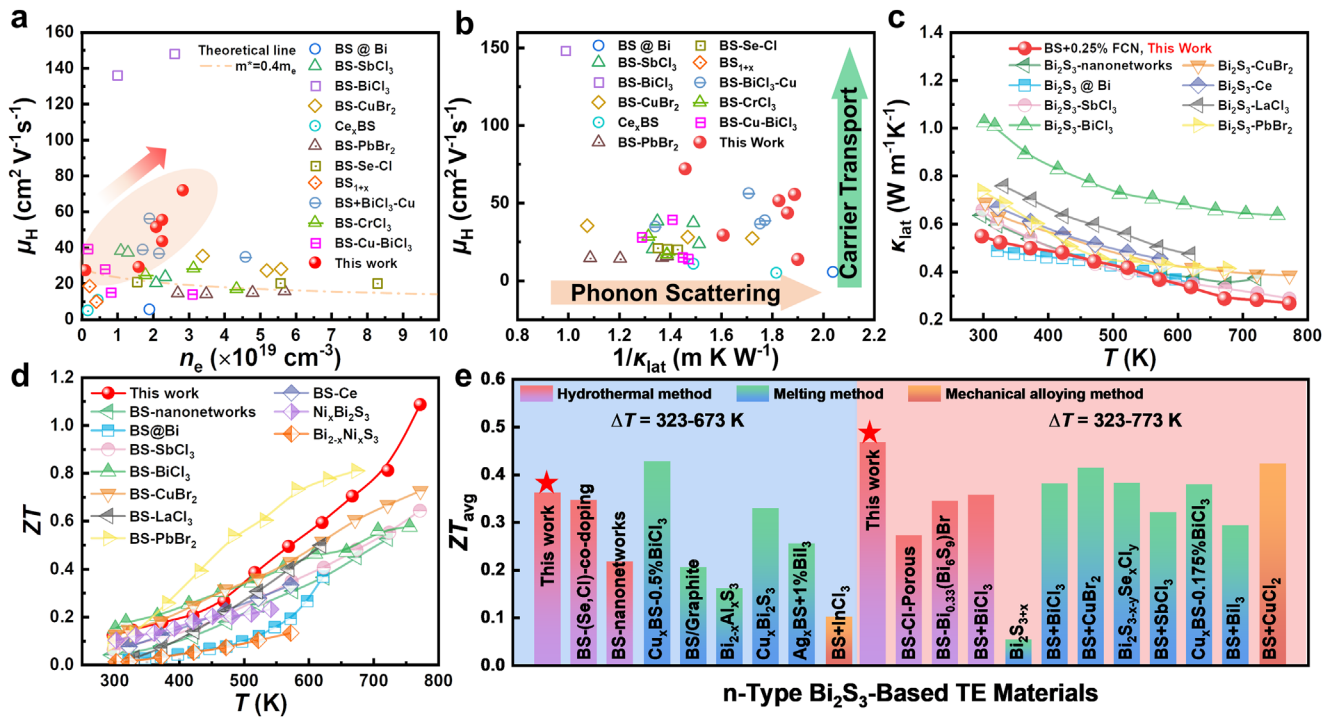


FIGURE 9 | (a) Carrier mobility as a function of carrier density and its comparison with other Bi_2S_3 -based samples. (b) Relationship between carrier mobility and the reciprocal of lattice thermal conductivity and its comparison with other Bi_2S_3 -based samples. (c) Lattice thermal conductivity of $\text{Bi}_2\text{S}_3 + 0.25 \text{ wt. \% FCN}$ sample in comparison with other Bi_2S_3 -based samples. (d) ZT of this work in comparison with other Bi_2S_3 -based samples and (e) ZT_{avg} of this work in comparison with other Bi_2S_3 -based samples at 323 – 673 K and 323 – 773 K ranges. Note that all comparative data cited in this figure are based on polycrystalline bulk materials. BS represents Bi_2S_3 for short.

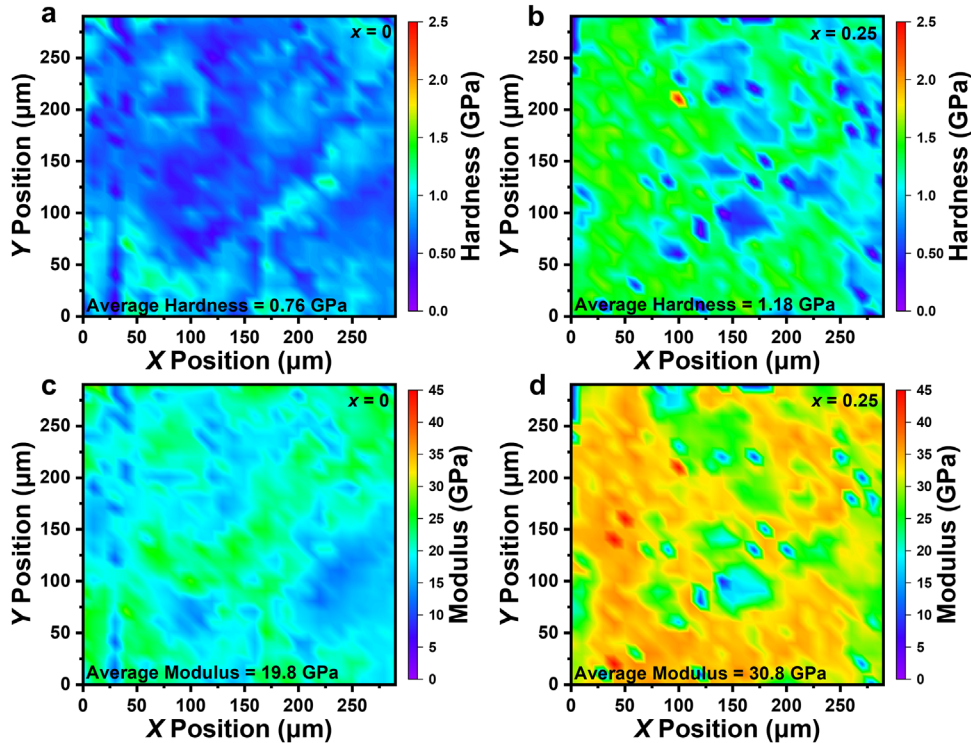


FIGURE 10 | 2D contour maps of (a,b) hardness and (c,d) Young's modulus for the pure Bi_2S_3 and $\text{Bi}_2\text{S}_3 + 0.25 \text{ wt. \% FCN}$ samples.

thermoelectric materials. Further investigations are therefore desirable.

3 | Conclusion

In conclusion, this study demonstrates a promising strategy that utilizes the difference in chemical activity between metal elements and the volatile nature of Bi to significantly improve the thermoelectric performance of n-type binary polycrystalline Bi₂S₃. Reaction between Bi₂S₃ with FCN powders during SPS results in effective incorporation of FCN to Bi₂S₃ lattice on the one hand. On the other hand, it leads to the reduction reaction that forms metallic Bi and FCN-S compounds within the FCN incorporated Bi₂S₃ matrix. The FCN incorporation and the conductive precipitate phases formed synergistically enhance n_e and μ_H . In combination with the significantly increased σ and the relatively high S values, a highly enhanced PF of about 551 $\mu\text{W m}^{-1} \text{K}^{-2}$ is obtained at 773 K for the Bi₂S₃ + 0.25 wt.% FCN sample. In parallel, the volatility of nanosized Bi during SPS triggers the formation of nanopores, which, in combination with the presence of multiscale lattice defects, contribute to the effective scattering of all-scale phonons in the whole temperature range and maintain a low κ_{lat} of 0.27 $\text{W m}^{-1} \text{K}^{-1}$ at 773 K for Bi₂S₃ + 0.25 wt.% FCN sample. Consequently, an excellent peak ZT of 1.1 is realized at 773 K in the n-type Bi₂S₃ + 0.25 wt.% FCN polycrystals, suggesting that Bi₂S₃ is a promising thermoelectric material for industrial applications. The strategy used in this study provides a valuable reference for other thermoelectric material systems.

4 | Experimental Section

The experimental details can be found in the Supporting information.

Acknowledgements

We thank the financial support from the National Natural Science Foundation of China (Grant No. 52562030), National Key R&D Program of China (Grant No. 2022YFF0503804), Academician (Expert) Workstation of Yunnan Province Program (Grant No. 202405AF140066), Yunnan Science and Technology Program (Grant No. 202401AT070403), Outstanding Youth Fund of Yunnan Province (Grant No. 202201AV070005), National Natural Science Foundation of China (Grant No. 52162029) and Yunnan Major Scientific and Technological Projects (Grant No. 202302AG050010).

Open access funding enabled and organized by Projekt DEAL.

Funding

National Natural Science Foundation of China (Grant No. 52562030), National Key R&D Program of China (Grant No. 2022YFF0503804), Academician (Expert) Workstation of Yunnan Province Program (Grant No. 202405AF140066), Yunnan Science and Technology Program (Grant No. 202401AT070403), Outstanding Youth Fund of Yunnan Province (Grant No. 202201AV070005), National Natural Science Foundation of China (Grant No. 52162029) and Yunnan Major Scientific and Technological Projects (Grant No. 202302AG050010).

Conflicts of Interest

The authors declare no conflict of interest.

Data Availability Statement

The data that support the findings of this study are available from the corresponding author upon reasonable request.

References

1. F. J. DiSalvo, "Thermoelectric Cooling and Power Generation," *Science* 285 (1999): 703–706, <https://doi.org/10.1126/science.285.5428.703>.
2. R. Y. Nuwayhid, A. Shihadeh, and N. Ghaddar, "Development and testing of a domestic woodstove thermoelectric generator With natural convection cooling," *Energy Conversion and Management* 46 (2005): 1631–1643, <https://doi.org/10.1016/j.enconman.2004.07.006>.
3. L. E. Bell, "Cooling, Heating, Generating Power, and Recovering Waste Heat With Thermoelectric Systems," *Science* 321 (2008): 1457–1461, <https://doi.org/10.1126/science.1158899>.
4. D. Liu, D. Wang, T. Hong, et al., "Lattice plainification advances highly effective SnSe crystalline thermoelectrics," *Science* 380 (2023): 841–846, <https://doi.org/10.1126/science.adg7196>.
5. Y. Qin, B. Qin, T. Hong, et al., "Grid-plainification enables medium-temperature PbSe thermoelectrics to cool better Than Bi₂Te₃," *Science* 383 (2024): 1204–1209, <https://doi.org/10.1126/science.adk9589>.
6. H. Liang, J. Guo, Y.-X. Zhou, Z.-Y. Wang, J. Feng, and Z.-H. Ge, "CuPbBi₅S₉ thermoelectric material With an intrinsic low thermal conductivity: Synthesis and properties," *Journal of Materiomics* 8 (2022): 174–183, <https://doi.org/10.1016/j.jmat.2021.03.016>.
7. Y. Jin, Y. Qiu, S. Bai, et al., "Modifying Roles of CuSbSe₂ in Realizing High Thermoelectric Performance of GeTe," *Advanced Energy Materials* 14 (2024): 2400623, <https://doi.org/10.1002/aenm.202400623>.
8. H.-N. Shi, S.-L. Bai, Y.-P. Wang, et al., "Contrasting strategies of optimizing carrier concentration in bulk InSe for enhanced thermoelectric performance," *Rare Metals* 43 (2024): 4425–4432, <https://doi.org/10.1007/s12598-024-02756-z>.
9. S. Zhan, S. Bai, B. Qin, et al., "High Carrier Mobility Promotes In-Plane Thermoelectric Performance of n-Type PbSnS 2 Crystals," *Advanced Functional Materials* 34 (2024): 2406428, <https://doi.org/10.1002/adfm.202406428>.
10. M. Li, X. Zhao, D. Wang, et al., "Enhancing the Thermoelectric and Mechanical Properties of p-Type PbS Through Band Convergence and Microstructure Regulation," *Nano Letters* 24 (2024): 8126–8133, <https://doi.org/10.1021/acs.nanolett.4c02058>.
11. X. Qian, H.-R. Guo, J.-X. Lyu, et al., "Enhancing thermoelectric performance of p-type SnTe Through manipulating energy band structures and decreasing electronic thermal conductivity," *Rare Metals* 43 (2024): 3232–3241, <https://doi.org/10.1007/s12598-024-02663-3>.
12. B. Qin, D. Wang, X. Liu, et al., "Power generation and thermoelectric cooling enabled by momentum and energy multiband alignments," *Science* 373 (2021): 556–561, <https://doi.org/10.1126/science.abi8668>.
13. T. Chen, S. Li, K. Chen, et al., "Enhancing Thermoelectric Performance of n-Type Bi₂Te_{2.7}Se_{0.3} Through Incorporation of Amorphous Si₃N₄ Nanoparticles," *ACS Applied Materials and Interfaces* 16 (2024): 22016–22024.
14. Z. Fan, J. Liang, J.-L. Chen, et al., "Realizing high thermoelectric performance for p-type SiGe in medium temperature region via TaC compositing," *Journal of Materiomics* 9 (2023): 984–991, <https://doi.org/10.1016/j.jmat.2023.03.004>.
15. J. Yu, X. Liu, H. Hu, et al., "Ultralow thermal conductivity and high ZT of Cu₂Se-based thermoelectric materials mediated by TiO_{2-n} nanoclusters," *Joule* 8 (2024): 2652–2666, <https://doi.org/10.1016/j.joule.2024.06.007>.
16. K. Jin, J. Tiwari, T. Feng, Y. Lou, and B. Xu, "Realizing high thermoelectric performance in eco-friendly Bi₂S₃ With nanopores and Cl-doping Through shape-controlled nano precursors," *Nano Energy* 100 (2022): 107478, <https://doi.org/10.1016/j.nanoen.2022.107478>.

17. W. Zhang, B. A. Al-Maythalyon, F. Gao, et al., "Thermally stable inorganic Bi_{0.4}Sb_{1.6}Te₃/metal-organic framework (MOF) composites With 1-by-1 nm pore engineering towards mid-temperature thermoelectrics," *Energy & Environmental Science* 17 (2024): 5679–5690, <https://doi.org/10.1039/D4EE01652A>.
18. Z. Yang, Y. Han, Y. Liang, et al., "Chalcogenide perovskite BaZrS₃ bulks for thermoelectric conversion With ultra-high carrier mobility and low thermal conductivity," *Acta Materialia* 276 (2024): 120156, <https://doi.org/10.1016/j.actamat.2024.120156>.
19. P.-F. Liu, X. Li, J. Li, et al., "Strong low-energy rattling modes enabled liquid-Like ultralow thermal conductivity in a well-ordered solid," *National Science Review* 11 (2024): nwae216, <https://doi.org/10.1093/nsr/nwae216>.
20. K. Guo, J. Zhang, X. Yu, et al., "In-Plane Overdamping and Out-Plane Localized Vibration Contribute to Ultralow Lattice Thermal Conductivity of Zintl Phase KcSb," *Advanced Science* 11 (2024): 2402209, <https://doi.org/10.1002/advs.202402209>.
21. F. Hao, P. Qiu, Y. Tang, et al., "High efficiency Bi₂Te₃-based materials and devices for thermoelectric power generation Between 100 and 300°C," *Energy & Environmental Science* 9 (2016): 3120–3127, <https://doi.org/10.1039/C6EE02017H>.
22. B. Zhu, X. Liu, Q. Wang, et al., "Realizing record high performance in n-type Bi₂Te₃-based thermoelectric materials," *Energy & Environmental Science* 13 (2020): 2106–2114, <https://doi.org/10.1039/D0EE01349H>.
23. Y.-K. Zhu, Y. Sun, X. Dong, et al., "General design of high-performance and textured layered thermoelectric materials via stacking of mechanically exfoliated crystals," *Joule* 8 (2024): 2412–2424, <https://doi.org/10.1016/j.joule.2024.05.006>.
24. H.-L. Zhuang, H. Hu, J. Pei, et al., "High ZT in p-Type Thermoelectric (Bi,Sb)₂Te₃ with Built-in Nanopores," *Energy and Environmental Science* 15 (2022): 2039–2048.
25. Y. Xiao, H. Wu, W. Li, et al., "Remarkable Roles of Cu To Synergistically Optimize Phonon and Carrier Transport in n-Type PbTe-Cu₂Te," *Journal of the American Chemical Society* 139 (2017): 18732–18738, <https://doi.org/10.1021/jacs.7b11662>.
26. H. J. Wu, L. D. Zhao, F. S. Zheng, et al., "Broad temperature plateau for thermoelectric figure of merit ZT>2 in phase-separated PbTe_{0.7}SO_{0.3}," *Nature Communications* 5 (2014): 4515.
27. B. Jiang, Y. Yu, J. Cui, et al., "High-entropy-stabilized chalcogenides With high thermoelectric performance," *Science* 371 (2021): 830–834, <https://doi.org/10.1126/science.abe1292>.
28. S. Cai, S. Hao, Z.-Z. Luo, et al., "Discordant nature of Cd in PbSe: Off-centering and core-shell nanoscale CdSe precipitates lead to high thermoelectric performance," *Energy & Environmental Science* 13 (2020): 200–211, <https://doi.org/10.1039/C9EE03087E>.
29. W. Li, L. Zheng, B. Ge, et al., "Promoting SnTe as an Eco-Friendly Solution for p-PbTe Thermoelectric via Band Convergence and Interstitial Defects," *Advanced Materials* 29 (2017): 1605887, <https://doi.org/10.1002/adma.201605887>.
30. Z. Li, X. He, H. Li, C. Wang, Y. Niu, and J. Jiang, "The effect of thermoelectric augmentation dramatically increased the specific capacity for electrochemical energy storage," *Chemical Engineering Journal* 495 (2024): 153535, <https://doi.org/10.1016/j.cej.2024.153535>.
31. J. Chen, Z. Dong, Q. Li, et al., "Enhanced Thermoelectric Performance in Vacancy-Filling Heuslers due to Kondo-Like Effect," *Advanced Materials* 36 (2024): 2405858, <https://doi.org/10.1002/adma.202405858>.
32. K. Biswas, L. D. Zhao, M. G. Kanatzidis, and T.-F. Thermoelectric, "The Anisotropic n-Type Semiconductor Bi₂S₃," *Advanced Energy Materials* 2 (2012): 634–638.
33. Z.-H. Ge, B.-P. Zhang, Y.-Q. Yu, and P.-P. Shang, "Fabrication and properties of Bi_{2-x}Ag_{3x}S₃ thermoelectric polycrystals," *Journal of Alloys and Compounds* 514 (2012): 205–209, <https://doi.org/10.1016/j.jallcom.2011.11.072>.
34. J. Yang, H. Ye, X. Zhang, et al., "Dual-Site Doping and Low-Angle Grain Boundaries Lead to High Thermoelectric Performance in N-Type Bi₂S₃," *Advanced Functional Materials* 34 (2024): 2306961, <https://doi.org/10.1002/adfm.202306961>.
35. J. Yang, L. X. Yu, T. T. Wang, et al., "Thermoelectric properties of n-type Cu Bi₂S₃ materials fabricated by plasma activated sintering," *Journal of Alloys and Compounds* 780 (2019): 35–40, <https://doi.org/10.1016/j.jallcom.2018.11.343>.
36. H. Liu, L. Zhang, Y. Shen, et al., "Enhanced thermoelectric performance of Bi_{2-x}Cu_xS₃ by hydrothermal synthesis and spark plasma sintering," *Ceramics International* 49 (2023): 36130–36136, <https://doi.org/10.1016/j.ceramint.2023.08.292>.
37. J. Pei, L. J. Zhang, B. P. Zhang, P. P. Shang, and Y. C. Liu, "Enhancing the thermoelectric performance of Ce_xBi₂S₃ by optimizing the carrier concentration combined With band engineering," *Journal of Materials Chemistry C* 5 (2017): 12492–12499, <https://doi.org/10.1039/C7TC04082B>.
38. W. Liu, C. F. Guo, M. Yao, et al., "Bi₂S₃ nanonetwork as precursor for improved thermoelectric performance," *Nano Energy* 4 (2014): 113–122, <https://doi.org/10.1016/j.nanoen.2013.12.015>.
39. B. Xu, T. Feng, M. T. Agne, et al., "Highly Porous Thermoelectric Nanocomposites With Low Thermal Conductivity and High Figure of Merit From Large-Scale Solution-Synthesized Bi₂Te_{2.5}Se_{0.5} Hollow Nanostructures," *Angewandte Chemie International Edition* 56 (2017): 3546–3551, <https://doi.org/10.1002/anie.201612041>.
40. H. Ju, K. Kim, D. Park, and J. Kim, "Fabrication of porous SnSeS nanosheets With controlled porosity and their enhanced thermoelectric performance," *Chemical Engineering Journal* 335 (2018): 560–566.
41. H. Hu, H.-L. Zhuang, Y. Jiang, et al., "Thermoelectric Cu₁₂Sb₄S₁₃-Based Synthetic Minerals With a Sublimation-Derived Porous Network," *Advanced Materials* 33 (2021): 2103633, <https://doi.org/10.1002/adma.202103633>.
42. K. P. Zhao, H. Z. Duan, N. Raghavendra, et al., "Solid-State Explosive Reaction for Nanoporous Bulk Thermoelectric Materials," *Advanced Materials* 29 (2017): 1701148.
43. C. B. Tang, Y. Liu, L. G. Ye, Y. M. Chen, M. T. Tang, and S. H. Yang, "Production of bismuth by directly reducing-matting smelting From bismuth sulfide concentrate," *Chin J Nonferrous Metals* 27 (2017): 363–370.
44. Z.-H. Ge, B.-P. Zhang, Z.-X. Yu, and J.-F. Li, "Effect of spark plasma sintering temperature on thermoelectric properties of Bi₂S₃ polycrystal," *Journal of Materials Research* 26 (2011): 2711–2718, <https://doi.org/10.1557/jmr.2011.273>.
45. R. B. Shalvoy, G. B. Fisher, and P. J. Stiles, "Bond ionicity and structural stability of some average-valence-five materials studied by x-ray photoemission," *Physical Review B* 15 (1977): 1680–1697, <https://doi.org/10.1103/PhysRevB.15.1680>.
46. J. Guo, Z. Ge, M. Hu, P. Qin, and J. Feng, "Facile Synthesis of NaBi₂ Nanoribbons as a Promising Visible Light-Driven Photocatalyst," *Physica status solidi (RRL)* 12 (2018): 1800135.
47. J. Guo, Q. Lou, Y. Qiu, et al., "Remarkably enhanced thermoelectric properties of Bi₂S₃ nanocomposites via modulation doping and grain boundary engineering," *Applied Surface Science* 520 (2020): 146341.
48. M. Guo, L. Zhou, Y. Li, Q. Zheng, F. Xie, and D. Lin, "Unique nanosheet-nanowire structured CoMnFe layered triple hydroxide arrays as self-supporting electrodes for a high-efficiency oxygen evolution reaction," *Journal of Materials Chemistry A* 7 (2019): 13130–13141, <https://doi.org/10.1039/C9TA01531K>.
49. Y.-G. Feng, H.-J. Niu, L.-P. Mei, J.-J. Feng, K.-M. Fang, and A.-J. Wang, "Engineering 3D hierarchical thorn-Like PtPdNiCu alloyed nanotriplets With enhanced performances for methanol and ethanol electrooxidation," *Journal of Colloid and Interface Science* 575 (2020): 425–432, <https://doi.org/10.1016/j.jcis.2020.04.120>.
50. J. Hao, Z. Zhuang, K. Cao, et al., "Unraveling the electronegativity-dominated intermediate adsorption on high-entropy alloy electrocata-

- lysts," *Nature Communications* 13 (2022): 2662, <https://doi.org/10.1038/s41467-022-30379-4>.
51. P. Brož, J. Vřešťál, J. Sopoušek, et al., "High entropy alloys (FeCoNi)_{0.75}Cr_{0.25-x}Cu_x – thermal stability and physical properties," *J Alloy Compd* 993 (2024): 174628.
52. S. Xiong, W. Qi, Y. Cheng, B. Huang, M. Wang, and Y. Li, "Universal relation for size dependent thermodynamic properties of metallic nanoparticles," *Physical Chemistry Chemical Physics* 13 (2011): 10652–10660, <https://doi.org/10.1039/c0cp90161j>.
53. A. Eremin and E. Gurentsov, "Evaporation temperature depression With decrease of iron nanoparticle size. Validation of semi-empirical models," *Materials Chemistry and Physics* 228 (2019): 180–186, <https://doi.org/10.1016/j.matchemphys.2019.02.052>.
54. T. H. Wang, Y. F. Zhu, and Q. Jiang, "Size effect on evaporation temperature of nanocrystals," *Materials Chemistry and Physics* 111 (2008): 293–295, <https://doi.org/10.1016/j.matchemphys.2008.04.010>.
55. J. Zhu, X. Zhang, M. Guo, et al., "Restructured single parabolic band model for quick analysis in thermoelectricity," *Npj Computational Materials* 7 (2021): 116, <https://doi.org/10.1038/s41524-021-00587-5>.
56. Y. Wen, Y. Liu, T. Wang, et al., "High-Mass-Loading Ni–Co–S Electrodes With Unfading Electrochemical Performance for Supercapacitors," *ACS Applied Energy Materials* 4 (2021): 6531–6541, <https://doi.org/10.1021/acsaem.1c00557>.
57. J. Hu, Y. Shi, L. Sun, et al., "MOF-derived spherical Ni S /carbon With B-doping enabling high supercapacitive performance," *Journal of Materials Science & Technology* 153 (2023): 219–227, <https://doi.org/10.1016/j.jmst.2022.11.065>.
58. X. Ren, Y. Zhou, Y. Du, et al., "Facile ion exchange to construct Ni-Fe-Co sulfides and hydroxides ultrathin nanosheets With rich interfaces for advanced all-solid-state asymmetric supercapacitors," *Applied Surface Science* 514 (2020): 145951, <https://doi.org/10.1016/j.apsusc.2020.145951>.
59. Y. Gao, X. Yue, Y. Dong, Q. Zheng, and D. Lin, "High-efficiency activated phosphorus-doped Ni₂S₃/Co₃S₄/ZnS nanowire/nanosheet arrays for energy storage of supercapacitors," *Journal of Colloid and Interface Science* 658 (2024): 441–449, <https://doi.org/10.1016/j.jcis.2023.12.099>.
60. G. J. Snyder, A. H. Snyder, M. Wood, et al., "Weighted Mobility," *Advanced Materials* 32 (2020): 2001537, <https://doi.org/10.1002/adma.202001537>.
61. H. S. Kim, Z. M. Gibbs, Y. L. Tang, H. Wang, and G. J. Snyder, "Characterization of Lorenz number With Seebeck coefficient measurement," *APL Materials* 3 (2015): 041506, <https://doi.org/10.1063/1.4908244>.
62. J. Guo, J. Yang, Z.-H. Ge, et al., "Realizing High Thermoelectric Performance in Earth-Abundant Bi₂S₃ Bulk Materials via Halogen Acid Modulation," *Advanced Functional Materials* 31 (2021): 2102838, <https://doi.org/10.1002/adfm.202102838>.
63. D. G. Cahill, S. K. Watson, and R. O. Pohl, "Lower limit to the thermal conductivity of disordered crystals," *Physical Review B* 46 (1992): 6131–6140, <https://doi.org/10.1103/PhysRevB.46.6131>.
64. J. Callaway and H. C. von Baeyer, "Effect of Point Imperfections on Lattice Thermal Conductivity," *Physical Review* 120 (1960): 1149–1154, <https://doi.org/10.1103/PhysRev.120.1149>.
65. R. Li, G. Wu, Q. Zhang, et al., "Robust (Bi,Sb)₂Te₃ Thermoelectrics Due to Engineered Ion Confinement and Microstructure for Advancing Thermoelectric Power Generators," *Advanced Functional Materials* 35 (2025): 2502535, <https://doi.org/10.1002/adfm.202502535>.
66. A. U. Khan, K. Kobayashi, D.-M. Tang, et al., "Nano-micro-porous skutterudites With 100% enhancement in ZT for high performance thermoelectricity," *Nano Energy* 31 (2017): 152–159, <https://doi.org/10.1016/j.nanoen.2016.11.016>.
67. J. Yang, J. N. Yan, G. W. Liu, Z. Q. Shi, and G. J. Qiao, "Improved thermoelectric properties of n-type Bi₂S₃ via grain boundaries and in-situ nanoprecipitates," *Journal of the European Ceramic Society* 39 (2019): 1214–1221, <https://doi.org/10.1016/j.jeurceramsoc.2018.11.053>.
68. Z. H. Liu, Y. L. Pei, H. Y. Geng, et al., "Enhanced thermoelectric performance of Bi₂S₃ by synergistical action of bromine substitution and copper nanoparticles," *Nano Energy* 13 (2015): 554–562, <https://doi.org/10.1016/j.nanoen.2015.03.036>.
69. J. Guo, Y.-X. Zhang, Z.-Y. Wang, et al., "High thermoelectric properties realized in earth-abundant Bi₂S₃ bulk via carrier modulation and multi-nano-precipitates synergy," *Nano Energy* 78 (2020): 105227, <https://doi.org/10.1016/j.nanoen.2020.105227>.
70. J. Guo, Z.-Y. Wang, Y.-K. Zhu, L. Chen, J. Feng, and Z.-H. Ge, "Synergistically enhanced thermoelectric properties of Bi₂S₃ bulk materials via Cu interstitial doping and BiCl₃ alloying," *Rare Metals* 41 (2022): 931–941, <https://doi.org/10.1007/s12598-021-01848-4>.
71. Y. Zhu, X. Wang, Y. Shen, Y. Xu, F. Du, and J. Yang, "High thermoelectric performance in n-type bismuth sulfide by carrier concentration tuning and dense nanodomains," *Journal of the European Ceramic Society* 44 (2024): 5096–5104, <https://doi.org/10.1016/j.jeurceramsoc.2024.02.025>.
72. Y. Chen, D. Y. Wang, Y. L. Zhou, et al., "Enhancing the thermoelectric performance of Bi₂S₃: A promising earth-abundant thermoelectric material," *Frontiers of Physics* 14 (2019): 013601, <https://doi.org/10.1007/s11467-018-0845-4>.
73. Y. Wu, J. Pei, R. Zhang, Z. C. Huang, Z. Zhao, and B. P. Zhang, "Temperature gradient cooling technique: Boosting high power factor of Bi₂S₃+ thermoelectric material," *Journal of Alloys and Compounds* 830 (2020): 154451, <https://doi.org/10.1016/j.jallcom.2020.154451>.
74. R. Fortulan, S. Aminorroaya Yamini, C. Nwanebu, et al., "Thermoelectric Performance of n-Type Magnetic Element Doped Bi₂S₃," *ACS Applied Energy Materials* 5 (2022): 3845–3853, <https://doi.org/10.1021/acsaem.2c00295>.
75. Z. H. Ge, P. Qin, D. S. He, et al., "Highly Enhanced Thermoelectric Properties of Bi/Bi₂S₃ Nanocomposites," *ACS Applied Materials and Interfaces* 9 (2017): 4828–4834.
76. Y. Wu, Q. Lou, Y. Qiu, et al., "Highly enhanced thermoelectric properties of nanostructured Bi₂S₃ bulk materials via carrier modification and multi-scale phonon scattering," *Inorganic Chemistry Frontiers* 6 (2019): 1374–1381, <https://doi.org/10.1039/C9QI00213H>.
77. F. Fitriani, S. M. Said, S. Rozali, et al., "Enhancement of Thermoelectric Properties in Cold Pressed Nickel Doped Bismuth Sulfide Compounds," *Electronic Materials Letters* 14 (2018): 689–699, <https://doi.org/10.1007/s13391-018-0072-8>.
78. W. Ji, H. Yu, X. Li, et al., "Influence of Ni doping on the thermoelectric properties of Bi₂S₃ via high pressure and high temperature," *Journal of Alloys and Compounds* 966 (2023): 171575, <https://doi.org/10.1016/j.jallcom.2023.171575>.
79. H. Hou, J. Yang, G. Liu, X. Zhang, and G. Qiao, "Effects of cation doping on thermoelectric properties of Bi₂S₃ materials," *Journal of Materials Science: Materials in Electronics* 33 (2022): 22291–22299.
80. J. Guo, Z. H. Ge, F. Qian, D. H. Lu, and J. Feng, "Achieving high thermoelectric properties of Bi₂S₃ via InCl₃ doping," *Journal of Materials Science* 55 (2020): 263–273, <https://doi.org/10.1007/s10853-019-04008-3>.
81. F. Anjum, P. Dixit, and T. Maiti, "Enhanced thermoelectric performance With improved mechanical strength in Bi₂S₃/graphite composites," *Carbon* 218 (2024): 118692, <https://doi.org/10.1016/j.carbon.2023.118692>.
82. J. N. Yan, J. Yang, B. Z. Ge, et al., "Effect of Silver and Iodine Co-doping on the Thermoelectric Properties of n-Type Bi₂S₃," *Journal of Electronic Materials* 48 (2019): 503–508, <https://doi.org/10.1007/s11664-018-6741-4>.
83. X. Yang, J. Guo, Z.-Y. Wang, et al., "Highly enhanced thermoelectric properties of Bi₂S₃ via (Se, Cl)-co doping in hydrothermal synthesis process," *Journal of Alloys and Compounds* 922 (2022): 166252, <https://doi.org/10.1016/j.jallcom.2022.166252>.
84. W. Ji, X.-L. Shi, W. Liu, et al., "Boosting the Thermoelectric Performance of n-type Bi₂S₃ by Hierarchical Structure Manipulation and

Carrier Density Optimization,” *Nano Energy* 87 (2021): 106171, <https://doi.org/10.1016/j.nanoen.2021.106171>.

85. J. Yang, G. W. Liu, J. N. Yan, X. Z. Zhang, Z. Q. Shi, and G. J. Qiao, “Enhanced the thermoelectric properties of n-type Bi₂S₃ polycrystalline by iodine doping,” *Journal of Alloys and Compounds* 728 (2017): 351–356, <https://doi.org/10.1016/j.jallcom.2017.08.148>.

86. W. Wang, S. J. Luo, C. Xian, et al., “Enhanced Thermoelectric Properties of Hydrothermal Synthesized BiCl₃/Bi₂S₃ Composites,” *J Inorg Mater* 34 (2019): 328–334.

87. J. Guo, Z.-Y. Wang, L. Chen, et al., “Bi_{0.33}(Bi₆S₉)Br compositing in Bi₂S₃ bulk materials forwards high thermoelectric properties,” *Physical Chemistry Chemical Physics* 24 (2022): 24290–24295, <https://doi.org/10.1039/D2CP02805K>.

Supporting Information

Additional supporting information can be found online in the Supporting Information section.

Supporting File: adma71998-sup-0001-SuppMat.docx